Automated detection and mapping of crystal tilt using thermal diffuse scattering in transmission electron microscopy

Mauricio Cattaneo [a,f], Knut Müller-Caspary [b,a,*], Juri Barthel [a,**], Katherine E. MacArthur [a], Nicolas Gauquelin [c], Marta Lipinska-Chwalek [a,e], Johan Verbeeck [c], Leslie J. Allen [d], Rafal E. Dunin-Borkowski [a]

[a] Ernst Ruska Centre (ER-C), Forschungszentrum Jülich GmbH, 52425 Jülich, Germany
[b] Department of Chemistry and Centre for NanoScience, Ludwig-Maximilians-University Munich, Butenandtstr. 11, 81377 Munich, Germany
[c] Electron Microscopy for Materials Science (EMAT), University of Antwerp, 2020 Antwerp, Belgium
[d] School of Physics, University of Melbourne, Parkville, Victoria 3010, Australia
[e] Central Facility for Electron Microscopy, RWTH Aachen University, 52074 Aachen, Germany
[f] 2nd Institute of Physics, RWTH Aachen University, 52074 Aachen, Germany

ARTICLE INFO

ABSTRACT

Quantitative interpretation of transmission electron microscopy (TEM) data of crystalline specimens often requires the accurate knowledge of the local crystal orientation. A method is presented which exploits momentum-resolved scanning TEM (STEM) data to determine the local mistilt from a major zone axis. It is based on a geometric analysis of Kikuchi bands within a single diffraction pattern, yielding the center of the Laue circle. Whereas the approach is not limited to convergent illumination, it is here developed using unit-cell averaged diffraction patterns corresponding to high-resolution STEM settings. In simulation studies, an accuracy of approximately 0.1 mrad is found. The method is implemented in automated software and applied to crystallographic tilt and in-plane rotation mapping in two experimental cases. In particular, orientation maps of high-Mn steel and an epitaxially grown $La_{0.7}Sr_{0.3}MnO_3$-$SrTiO_3$ interface are presented. The results confirm the estimates of the simulation study and indicate that tilt mapping can be performed consistently over a wide field of view with diameters well above 100 nm at unit cell real space sampling.

1. Introduction

Scanning transmission electron microscopy (STEM) has established itself as a method for structural characterization as well as chemical composition mapping with atomic-scale resolution. A diversity of imaging techniques has been developed, such as annular dark field (ADF) imaging providing Z-contrast [1], bright field (BF) and annular bright field (ABF) imaging of light elements [2], elemental mapping using electron energy-loss spectroscopy (EELS) [3] and energy-dispersive X-ray spectroscopy (EDX) [4].

Common to these methods is a signal dependence on the crystallographic orientation of the specimen with respect to the incident electron beam. Even relatively small mistilts away from a crystal zone axis can affect the dynamical scattering of the electron wave significantly [5–7]. Quantitative conclusions can often be drawn only via the comparison of experimental data with accompanying simulations,

which require accurate tilt information as input to model scattering dynamics realistically. In the case of EDX spectroscopy, for example, a deliberate sample tilt is applied in order to suppress electron channeling [8,9]. Furthermore, structure retrieval by, e.g., inverse multislice [10–13] can benefit either from the knowledge of local tilt as initial input, or as a sanity check of the reconstruction result.

Furthermore, research partly focuses on the local tilt distribution itself. Examples include materials where local variations of the orientation due to, e.g., stacking faults, interfaces, dislocations and grain boundaries are related to materials properties such as elasticity or ferroelectricity [14–16]. A technique to measure and map the local sample tilt would thus be beneficial for such applications, in particular if the data providing tilt information can be acquired simultaneously with, e.g., spectroscopic or Z-contrast data. In this regard, the advent of momentum resolution in STEM using ultra-fast cameras [17–22]

has dramatically expanded the versatility and flexibility of STEM, as complete diffraction patterns can be acquired at each scan position up to a certain spatial frequency. In that respect, four-dimensional STEM (4D-STEM) data sets have already been used to determine specimen tilt and thickness in an automated way by means of neural networks analyzing the elastic scattering signal [23]. Moreover, a correlative approach comparing mainly the elastic scattering signal in experimental and simulated position-averaged convergent beam electron diffraction (PACBED) patterns has also shown a high sensitivity to sample mistilt [24]. Because these approaches are crystal and zone axis specific, they require prior knowledge. In the method presented here, the amount of needed prior information is significantly reduced while maintaining a high evaluation speed and accuracy.

At least for specimens investigated at sufficiently large thicknesses and temperatures, typically above 10 nm at 300 K, thermal diffuse scattering (TDS) constitutes a considerable fraction of the dark-field intensity. Besides the smooth diffuse background, Kikuchi bands can be observed in diffraction patterns of crystals at high scattering angles [25]. Since Kikuchi bands are aligned with reciprocal lattice planes, their exploitation to measure crystal tilt is widespread in electron diffraction. For example, crystallographic orientation mapping via Kikuchi bands has a long tradition in scanning electron microscopy (SEM) using electron back-scatter diffraction (EBSD) [26–31]. In addition, orientation measurement and mapping based on Kikuchi or spot diffraction patterns has also been developed for the field of TEM, or transmission-SEM [32–38] The kernel of the existing Kikuchi band detection schemes in EBSD usually involves a Hough transform to locate the Kikuchi band crossings. However, Hough-based methods [39,40] can become imprecise in cases where rectangular-shaped Kikuchi bands do not constitute the dominant features in diffraction patterns. A strong zero-order Laue zone in diffraction patterns recorded in transmission significantly complicates the application of Hough transforms, especially at high beam energies in the (S)TEM.

In this work, we present an alternative approach based on Kikuchi band recognition from azimuthal intensity profiles in an annular dark-field region of a diffraction pattern. In earlier work, data of first-order Laue zones have been analyzed by azimuthal profiles as well, however, focusing on unidirectional atom position modulations [41]. While requiring only a minimum of input, such as the expected number of strong Kikuchi bands, the method performs very robustly in typical high-resolution STEM scenarios in, or close to, zone-axis orientation and allows us to quantify mistilt with well below 1 mrad accuracy and precision. Whereas, methodologically, each diffraction pattern is treated independently, the application of this scheme also provides the ability to map local tilts in large 4D STEM data sets. The procedure was implemented in a computer program to run fully automatically and computationally efficiently, such that the detection of the center of the Laue circle takes on the order of several milliseconds per diffraction pattern on current personal computer hardware.

In the following, the method to measure the tilt between a crystal axis and the incident beam direction based on single diffraction patterns is introduced conceptually. Major steps of the analysis include the enhancement of Kikuchi band contrast in the dark-field region using a renormalization scheme, the identification of Kikuchi band crossings from azimuthal profiles, as well as iteratively eliminating systematic errors arising from the initially unknown center of the Laue circle. That Frozen phonon multislice simulation studies are performed in order to assess accuracy and precision of the method in dependence on electron dose and mistilt. The method is then applied to two experimental cases demonstrating tilt mapping (1) across a large field of view spanning more than 100 nm in a bent cross-section containing an $La_{0.7}Sr_{0.3}MnO_3/SrTiO_3$ interface, and (2) to a smaller scale of approximately 10 nm across a twin boundary in high-Mn steel. For both examples, 4D-STEM data sets were recorded with atomic column resolution. Before the tilt analysis, the diffraction patterns were averaged over scan areas corresponding to the size of one projected unit
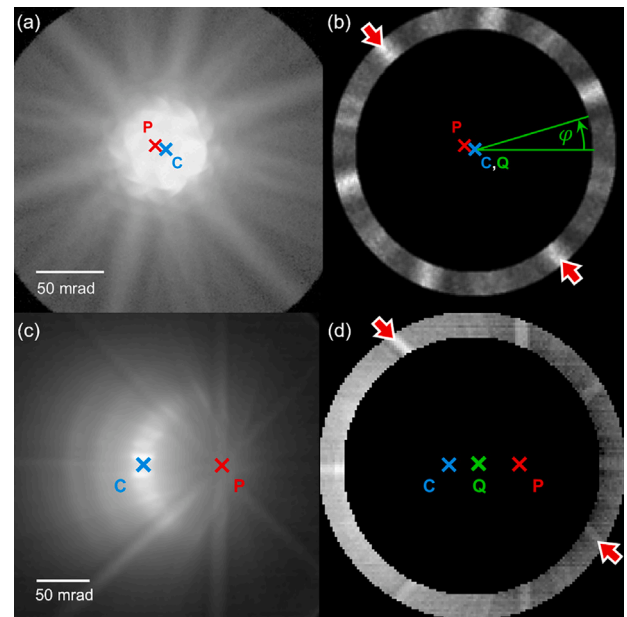
Fig. 1. (a) Diffraction pattern of a steel sample recorded with 300 keV electrons and at 7.2 mrad mistilt from the [110] zone axis. Kikuchi bands intersect in point **P** whereas the incident beam direction corresponds to point **C**. The logarithm of intensity is plotted to enhance the visibility of Kikuchi bands. (b) Re-normalized signal of the pattern in (a) within an annular region that is centered around the point **Q** = **C**. (c) Diffraction pattern of a SrTiO$_3$ sample recorded with 300-keV electrons at a large mistilt of about 75 mrad from the [100] zone axis. (d) Signal of the pattern in (c) within an annular region around **Q** in the detector center. Arrows indicate two traces of one Kikuchi band in the annular mask.

cell. Mistilt maps are thus generated from PACBED patterns with unit cell sampling. Due to the robustness and accuracy of the method, small changes of sample tilt are resolved over a large field of view as well as with high sampling close to interfaces and grain boundaries.

2. Methods

2.1. Conceptual outline and problem statement

The measurement of sample mistilt from a zone axis orientation based on Kikuchi bands, as proposed here, consists of locating the crossing point of the bands by geometrical construction and determining its distance from the center of the bright-field disc. In principle, this analysis could be performed exploiting the full information on tilt present in a two-dimensional diffraction pattern, e.g., by cross-correlation against an expected band pattern. However, the intensity distribution and details like the shape and width of Kikuchi bands depend on the crystal structure, sample thickness, zone-axis orientation, and further experimental parameters. This means a full two-dimensional analysis of the Kikuchi-band pattern obtained in transmission electron diffraction which would require extensive information as input to an automated routine. Since we are aiming for a fast method which requires only a minimum of prior knowledge, the evaluation approach is simplified by determining points in the diffraction plane through which Kikuchi bands pass.

In a preliminary step, an annular mask is applied to the diffraction pattern so as to separate the data including thermal diffuse scattering (TDS) and thus Kikuchi bands at medium to high angles from the bright field and low-angle diffraction. An example with a relatively small mistilt of 7.2 mrad is shown in Fig. 1(a, b) for the full and masked experimental diffraction pattern, respectively. In the following, we denote the locations of the undiffracted beam by **C**, the center of the Laue circle by **P** and the center of the annular mask by **Q**. As indicated

by the arrows in Fig. 1(b), Kikuchi bands passing through the mask leave two traces at approximately opposite sides of the annulus with azimuths differing by approximately π. Fig. 1(c, d) shows an example with a comparably large mistilt of 75 mrad, and a ring mask that is neither centered around **C** nor **P**. In such cases, the azimuth difference corresponding to a single Kikuchi band can deviate significantly from π. Moreover, the centering of the mask away from **C** leads to a strongly varying mean scattered intensity in dependence of the azimuth φ, and the traces of two bands can become very close and might even overlap in some cases. In addition, there can be a much higher intensity close to the inner rim of the mask.

These circumstances complicate an automatic and robust detection of Kikuchi bands by determining the azimuthal positions of their traces in the annular mask. Furthermore, the signal itself decreases along the radial direction, i.e. towards larger scattering angles where it approaches a Rutherford type of decay of the scattering cross-section [42]. This would inherently increase the weight of scattering close to the inner rim of the annulus if not corrected for during the evaluation. In that respect, it is noteworthy that the azimuthal resolution increases with the distance from the mask center. In the following, solutions to these problems are described which provide an enhancement of the Kikuchi-band signal, facilitate locating band positions within the annular region, and finally enable the determination of the position of the common band crossing, that is, the center of the Laue circle.

2.2. Enhancing Kikuchi band contrast

Since Kikuchi bands are not a dominant feature in the bright field and also in the low-angle dark-field region, a short camera length is beneficial for accessing large scattering angles such that the Bragg reflections within the zero-order Laue zone in the center cover less than a quarter of the recorded diffraction pattern, as shown by the examples in Fig. 1. For a given camera length and diffraction projection on the pixelated detector, we assume that both Kikuchi-band crossing **P** and bright field **C** are inside the inner radius of the annular mask. Consequently, the geometrical approach developed in the following is restricted to tilt variations limited by the inner radius of the annular mask at the present stage. However, since this already covers several tens of milliradians tilt variation, it is applicable to the majority of practically relevant cases. The outer radius of the mask is made as large as possible reaching out to the edge of the detector area.

Before an azimuthal scan is extracted from the area selected by the annular mask, the mask is partitioned in concentric rings of widths between one and two detector pixels. For each thin annular partition, the mean value of intensity is subtracted and the remaining signal variation is normalized with respect to the standard deviation. Each partition is then of equal strength in signal variation. For the subsequent integration of the signal along the radial direction, this renormalization avoids stronger weight of inner parts of the annular mask compared to outer parts due to the decay of the electron scattering cross-section towards larger angles. The result of renormalization within the annular mask is shown in Figs. 1(b) and (d), where the Kikuchi bands show only weak intensity variation along the radial direction, but a strong variation occurs azimuthally.

2.3. Azimuthal scan and Kikuchi band detection

A one-dimensional azimuthal intensity profile depending on φ is extracted from the annular mask by integrating the renormalized data along the radial direction. Sufficient azimuthal sampling is given, for example, by the number of pixels crossed by the inner circle limiting the annular mask. For each azimuthal sample the intensity is effectively integrated over a larger azimuthal range (1) in order to suppress the fine structure of Kikuchi bands which could possibly impede subsequent peak finding and (2) to further improve signal-to-noise ratio. The size of these azimuthal sectors should be close to the size of the Kikuchi
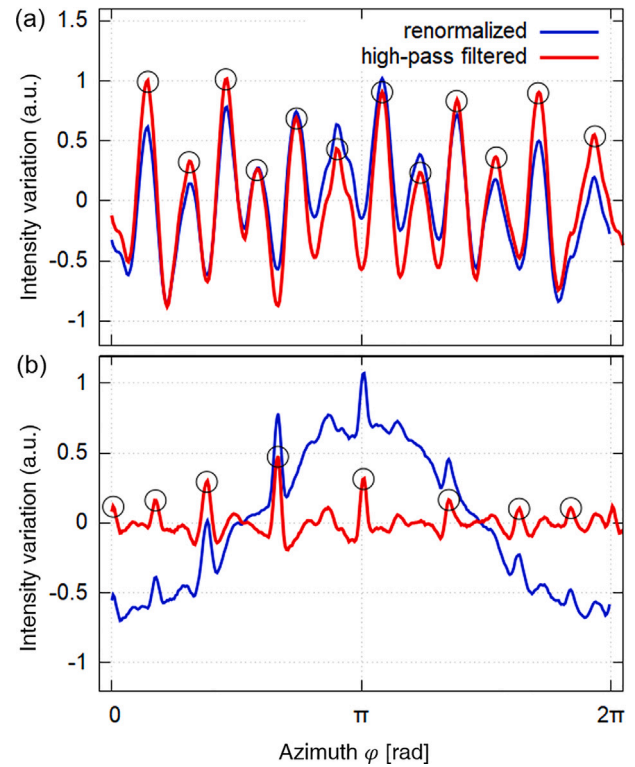

Fig. 2. Azimuthal scan (a) as extracted from the [110] steel diffraction pattern in Fig. 1(b) and (b) as extracted from the [100] SrTiO$_3$ pattern in Fig. 1(d). The azimuthal sampling was done in steps of one degree and binning into sectors spanning six degrees (blue curves). Kikuchi bands appear as narrow peaks in the profile. A strong background modulation is present because parts of the azimuthal scan are closer to the bright field than others. This background modulation is removed in the red curves by means of a high-pass filter. Black circles indicate the result of local peak detection.

bands within the annular mask. In that respect, sectors spanning five to ten degrees were found to be good choices in all cases analyzed so far.

Fig. 2(a) shows the azimuthal scan that has been directly extracted from the pattern in Fig. 1(b) in blue, using sectors with a width of six degrees. The three major and three minor Kikuchi bands in this pattern add up to twelve peaks in total. The azimuthal positions of the peaks are measured by detecting the local maxima, and the mean radius of the annular mask is used as radial position.

The azimuthal profile in Fig. 2(b) has been extracted directly from the example with larger mistilt in Fig. 1(d). It shows a strong one-fold, low-frequency modulation with an amplitude similar to that of the set of peaks caused by Kikuchi bands which impedes robust automatic peak detection and stems from the large deviation of **Q** from **C**. Such a low-frequency modulation is also present in the blue curve of Fig. 2(a), although with a much lower amplitude. A higher intensity occurs for azimuths where the mask is closer to the bright field and covers lower scattering angles. Besides difficulties in automated peak detection, this effect causes a significant shift of peaks located at strong slopes of the background. In order to prevent systematic errors arising from this effect, a high-pass filter is applied to the azimuthal scan which effectively removes the low-frequency background. This high-pass filter sets the lowest-order Fourier coefficients to zero resulting in the red profiles in Fig. 2, which are now dominated by the peaks caused by Kikuchi bands in terms of signal variation.

The black circles in Fig. 2(a) indicate the positions of the twelve strongest local maxima of the red curve expected for six Kikuchi bands in the case of a steel sample investigated close to [110] orientation. Likewise, the eight highest local maxima occurring in the red curve of Fig. 2(b) mark the locations expected from four strong Kikuchi bands

for [100] SrTiO$_3$. In the example of Fig. 2(a), peaks have comparable heights, stand out significantly from the background and can hence be detected straight forwardly by established methods. However, the situation is different for the high-pass filtered azimuthal profile in Fig. 2(b) which shows a large number of local maxima at azimuths not related to the centers of Kikuchi bands. A classification of a local maximum as a Kikuchi band or as a peak caused by noise related to, e.g., low counting statistics, is not obvious even for a human observer at least in some cases. For example, setting a threshold based on peak height, width, area or any other quantity regarded as peak strength, may easily reject actual Kikuchi-bands while accepting noise-related peaks. Therefore, the detection routine is allowed to find more than the expected number of local maxima and registers them in a sorted list by means of a parameter of strength, e.g. by the peak height. This approach allows for the identification of falsely detected peaks in the next step, based on a criterion that leads to the expected geometrical situation of Kikuchi bands, namely that they are crossing in one point of the diffraction pattern. Finally, note the regular spacing of peaks in Fig. 2a due to the nearly coinciding centers **P** and **Q** in Fig. 1b, as well as the distorted spacings of maxima on the φ axis in Fig. 2b where the mask centering deviates significantly from the center of the Laue circle according to Fig. 1d.

2.4. Determination of the Kikuchi band intersection

For n Kikuchi bands in a diffraction pattern the annular mask is ideally crossed twice by each band, generating $2n$ peaks in the azimuthal scan. In such cases, a straightforward approach to associate peak pairs to Kikuchi bands, is to connect one peak with the nth peak in the azimuthal sequence by a straight line. Thus n lines are constructed which have in total

$$\eta = \frac{n(n-1)}{2} \tag{1}$$

crossings, of which all coincide at or close to the center of the Laue circle in the ideal situation, as shown by the blue markers in Fig. 3. The procedure to calculate the crossing point for two pairs of different azimuths is detailed in Appendix.

This procedure relies entirely on the correct detection of all peaks and, in particular, of the complete set of pairs of peaks related to the Kikuchi bands. The association of peaks to pairs based on the azimuthal sequence fails to produce a set of crossing points forming a compact cloud, if Kikuchi bands are only partially detected. For example, this can happen if only one of the two intersections of a band with the annular mask is found, if two bands overlap and produce only one instead of two peaks, or when a false recognition occurs due to detecting peaks arising from noise. An example for a false relation of points to Kikuchi bands is shown by the red markers in Fig. 3, where only one of the two intersections of weak bands with the annulus were included. This leads to a false sequential association of pairs and thus to a wide scatter of crossing points quite far away from the common crossing of Kikuchi bands. The residual scatter of the crossing points for a correct selection of peaks is smaller and expected to be in the range of the width of Kikuchi bands.

In most cases, the set of the $2n$ strongest peaks found in the azimuthal scan provides also the best solution, especially when there are n Kikuchi bands that are clearly visible and sample mistilt is low. In order to stabilize the solution for more challenging scenarios, as the one shown in Fig. 3, more than $2n$ peaks are taken into consideration. In particular, the list of peaks found in the azimuthal scan is sorted with respect to the peak height, and extended to include also weaker ones which are only potentially related to Kikuchi bands. Several sets of $2n$ peaks are created from this extended list by randomly exchanging mostly weaker peaks. From these sets, the one leading to the lowest scatter of crossing points is chosen as the solution to identify the location of the Kikuchi-band crossing.
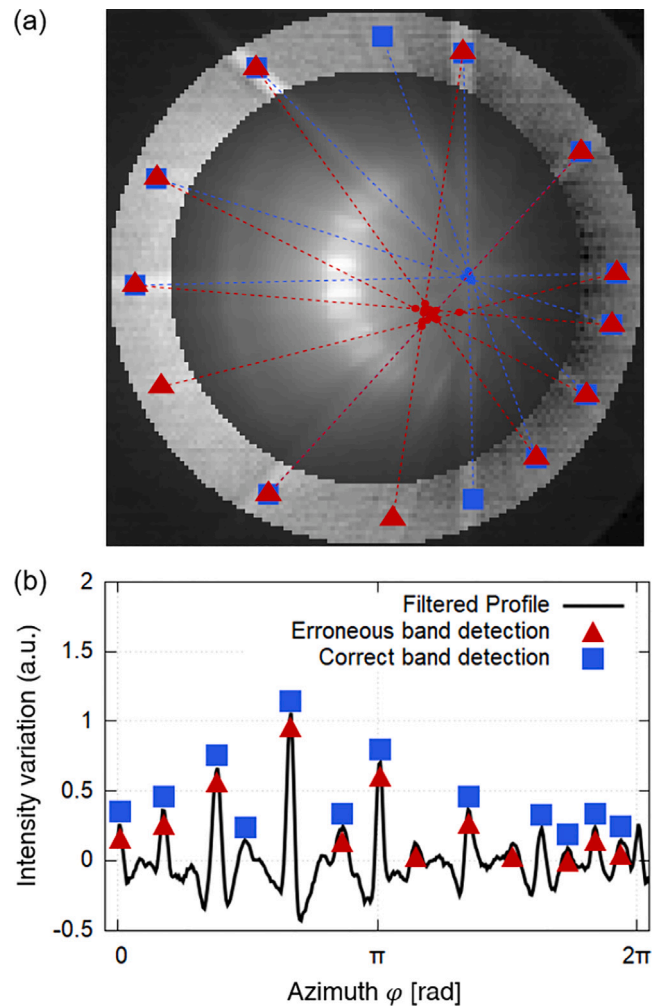

Fig. 3. (a) PACBED pattern of [110] fcc steel with larger mistilt and (b) azimuthal scan demonstrating an erroneous (red) and a correct (blue) association of detected peaks to pairs, which are assumed to represent the two traces of Kikuchi bands in the annular mask. The pairs deduced from the list of peaks marked by red triangles lead to the wrong result because the second trace of two Kikuchi bands is not included. The resulting set of crossing points shows a large scatter and is far away from the crossing point of the Kikuchi bands. The list of peaks marked by blue squares leads to a set of crossing points with low scatter at the crossing point of the Kikuchi bands.

2.5. Iterative error correction

On startup of the evaluation procedure, the position **P** of the center of the Laue circle in a diffraction pattern is unknown. Especially in the case of large sample mistilt, i.e. for a large distance between points **P** and **C** in Fig. 1, the annular mask applied in the previous steps will usually be centered around a point **Q** in the diffraction pattern that may be rather remote from the initially unknown point **P**. Consequences are that (1) Kikuchi bands are more difficult to resolve in parts of the mask close to **P** and (2) some bands cause peaks with an asymmetric shape in the azimuthal profile. The first issue can lead to a serious lack of detected pairs, whereas the second one causes a small systematic shift of the result towards the center of the mask. The two problems are illustrated schematically in Fig. 4 with two bands and a significant offset of their crossing from the center position of the annular mask. Errors due to these issues can be quite significant, i.e. larger than the scatter of crossing points found in the previous step.

The two problems described above are minimum if the annular mask is centered at the crossing of Kikuchi bands. Therefore, an iterative scheme is applied in which the annular mask is centered to the
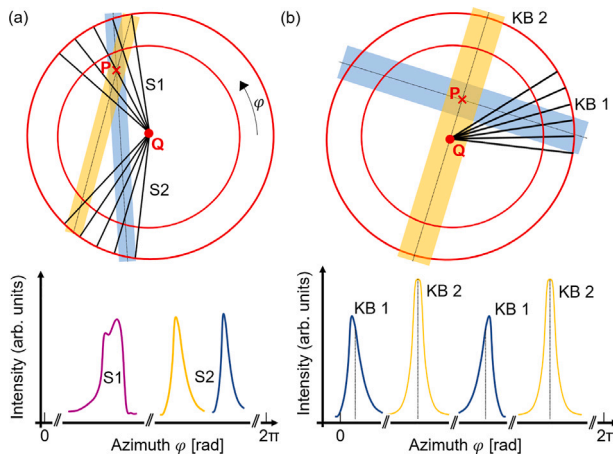
Fig. 4. Illustration of systematic errors in Kikuchi band detection due to an off-centered annular mask or significant sample mistilt. (a) Situation showing two bands crossing under a small angle close to the edge of the annular mask, which makes it difficult to resolve their intersections with the annulus in region "S1", whereas two well separated band sections occur in the opposite region "S2". (b) Situation with two perpendicular Kikuchi bands, where the band labeled "KB 1" is shifted off the mask center along band "KB 2". Symmetric peaks are registered in azimuthal sectors for "KB 2", which crosses the annular mask along the radial direction. In contrast, the peaks due to "KB 1" are asymmetric, which leads to a systematic shift of the deduced crossing point.

result of the previous evaluation and a new evaluation is performed. In most cases only one or two iterations are needed until the correction of the mask position is smaller than the scatter of crossing points.

2.6. Software implementation

The evaluation procedure described above has been implemented in a computer program using the C++ language. With commercial hardware, each iteration of finding a Kikuchi intersection for a single PACBED takes on the order of ten milliseconds using a single CPU thread. Parallel programming via OpenMP is applied to further speed up the analysis making use of the fact that the evaluation of multiple diffraction patterns can be performed independently. A set of 1000 diffraction patterns is evaluated by four threads in less than 25 s.

The program can take one or multiple diffraction patterns as input in form of two-dimensional arrays of intensity values together with parameters describing the size of the array. The inner radius limiting the annular mask and the number of expected Kikuchi bands n are the required input ensuring stability of the procedure. Defining the outer radius of the annular mask is optional but limiting the width of the annulus has shown improved performance in some cases. Output is the position of the Kikuchi band intersection P_N in the input array as determined after N iterations and an error estimate for the position corresponding to the root-mean-square deviation of all crossing points of detected Kikuchi bands. The mistilt is then calculated as the distance of the output position P_N to the known position C of the incident probe direction considering scaling parameters which describe the diffraction projection in physical units, e.g. in milliradians per pixel.

3. Simulation studies

In order to assess the accuracy and precision of the mistilt measurement, diffraction patterns were simulated using the multislice method [43] as implemented in the Dr. Probe software [44] for a large range of mistilts. Thermal diffuse scattering was simulated according to the quantum excitation of phonons (QEP) model [45] assuming an Einstein model of uncorrelated thermal vibration. As a test case, diffraction patterns were calculated for 40 nm thick fcc Fe viewed along the [110] zone axis based on the model of Straumanis & Kim [46].

An aberration-free incident electron probe of 200 keV kinetic energy and 25 mrad convergence semi-angle was assumed. PACBED patterns were obtained by summation of patterns resulting from more than 100 probe positions distributed uniformly over the projected unit cell. The diffraction patterns extend out to scattering angles of about 250 mrad due to a fine sampling of the supercell of 5×7 unit cells with 800×800 points perpendicular to the incident beam direction. The grid x-axis was along the $[\bar{1}10]$ direction and its y-axis along [001]. This setup also realizes a step size of approximately 1 mrad in the diffraction patterns, which is on the order of magnitude that can be achieved with fast pixelated direct electron detectors and convenient camera lengths in experiments. The potentials were projected along [110] within volume slices that are thin enough to contain just one atomic layer. For each layer 100 positional configurations were calculated by including random displacements with mean squared amplitudes of $\langle u^2 \rangle = 0.007 \text{ Å}^2$ [47]. By random selection of positional configurations from the pre-calculated set for each slice during the propagation of the probe function through a thick crystal in the multislice scheme, the scattering for each probe position is essentially calculated with an individual positional configuration. The summation of patterns from many probe positions form a PACBED pattern which thus also includes a summation over positional configurations achieving convergence for the signal related to thermal diffuse scattering. A pattern calculated in this way shows three strong Kikuchi bands along the main reciprocal lattice plains and weaker bands in between.

Test mistilts were distributed uniformly over a range up to 40 mrad tilt magnitude. Patterns obtained directly from the simulations correspond to infinite dose conditions. Scenarios representing a finite dose were simulated by adding noise following Poisson statistics. The total dose assumed in the simulation of one PACBED pattern translates to incident probe currents where we assume here a dwell time of 1 ms per probe position and 100 probe positions contributing to each simulated PACBED.

The histograms in Fig. 5 show the radial component of the mistilt detection error (a) without and (b) with iterating the tilt measurement using the result of one cycle as a start for the next. Without iteration a systematic error of approximately −0.2 mrad occurs, which might already be tolerable for many applications. The measurement becomes perfectly accurate if the iterative scheme is applied, since the distribution is symmetric around zero. This behavior of the automated evaluation procedure is independent of noise added due to a finite electron dose. Also the width of the distributions plotted in Fig. 5 shows no strong dependence on electron counting noise but is reduced by the iterative scheme. A precision of about ±0.13 mrad is deduced from the range containing 68% of the test cases, corresponding to the 1-σ level of a normal distribution. A slight decrease of the precision is found for the lowest probe current of 10 pA assumed in the simulations. Reduction of the incident probe current by another order of magnitude leads to a failure of the evaluation in over 50% of the cases under the applied conditions of the test, since the low signal of the Kikuchi bands could not be distinguished from noise anymore. It should be noted though that the probe current given in this test is not a fundamental limit because the signal-to-noise ratio of the Kikuchi bands also depends on the detection dwell-time, the size and efficiency of detector pixels, as well as the number of probe positions included in a PACBED. This means that the automated tilt measurement can also be applied in cases with lower probe currents or in low-dose experiments by averaging over a larger area of the scan field and by applying pattern binning.

4. Experimental results

4.1. Data acquisition

Experimental data has been acquired with an FEI Titan 80-300 [48] and an FEI Titan G2 80-200 [49] electron microscope at accelerating

(a) without refinement
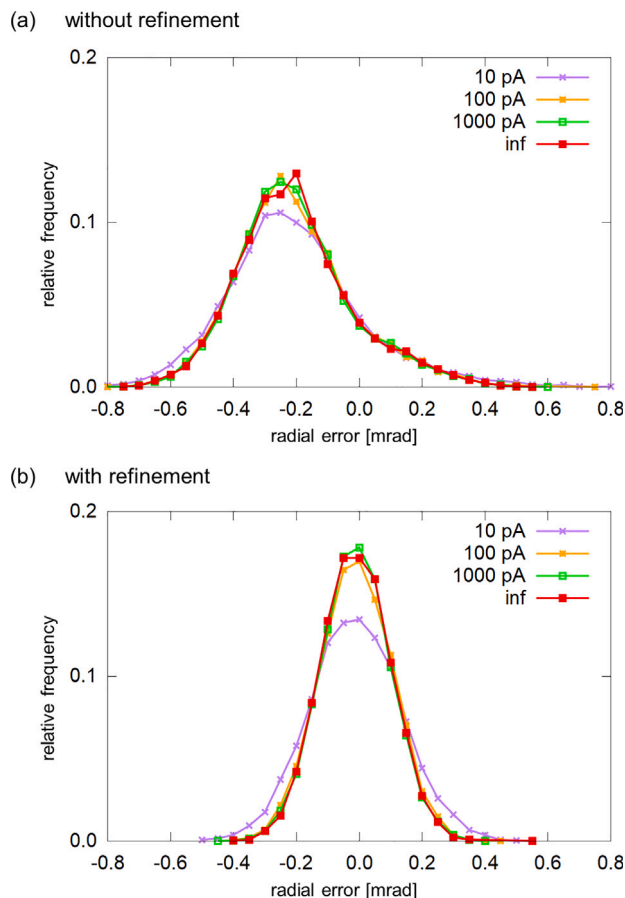
(b) with refinement

Fig. 5. Histograms of the overall radial error of mistilt measurements with simulated patterns for different probe currents. (a) Detection error for a direct evaluation, without iterative refinement. A systematic error of approximately 0.1 mrad is observed. (b) Improved accuracy after iterative refinement showing no significant systematic error.

voltages of 300 and 200 kV, respectively. The probe convergence semi-angle was limited to 25 mrad by an aperture and probe aberrations were minimized within this angular range using a double-hexapole corrector providing below 0.1 nm spatial resolution.

Momentum-resolved STEM data of a $La_{0.7}Sr_{0.3}MnO_3$ epitaxial layer grown on an $SrTiO_3$ substrate was recorded with a Merlin for EM Medipix 3 single chip detector (Quantum Detectors, Oxfordshire, UK) with a 256×256 pixel array [18,50]. The TEM sample was prepared by focused ion beam (FIB) milling in cross-section geometry. A second experimental case study of high-Mn steel has been performed using an electron microscope pixel array detector (EMPAD) (Thermo Fisher Scientific) with 128×128 pixels [21]. The TEM sample was prepared by a lift-out method in a dual-beam focused ion beam (FIB) FEI Helios NanoLab 460F1 [51].

In order to demonstrate the applicability of the method in practice, we present two case studies in the following. Firstly, it is shown that specimen bending occurring in thin foils of a perovskite heterostructure can be quantified at large fields of view (FOV). This example also shows that atomically resolved 4D-STEM with 10^6 scan pixels is feasible despite a slow frame rate in the kHz range, i.e. for a total scan time on the order of 1000 s. Secondly, we consider a perfect twin boundary in a high-Mn steel specimen. Since this interface is purely crystallographic, it exhibits no compositional or strain gradients but an in-plane rotation between the adjacent grains. Observations made in this example provide information about the spatial resolution of the method.
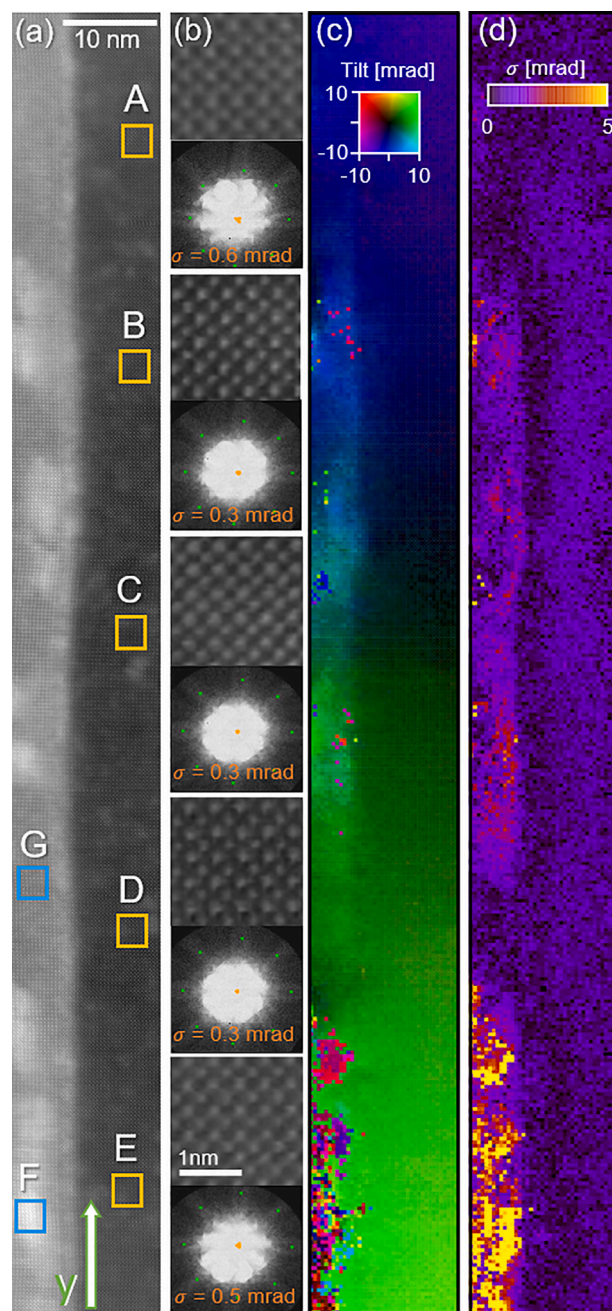
Fig. 6. Momentum-resolved STEM acquisition of epitaxial $La_{0.7}Sr_{0.3}MnO_3$ (bright layer, left) on $SrTiO_3$ (right). (a) Virtual detector ADF image of a 17×146 nm scan. (b) Five selected areas (green) from (a) with real space scan images and corresponding PACBED patterns. Green and yellow dots in the PACBEDs mark detected Kikuchi bands and deduced band crossings. The r.m.s. scatter σ of crossing points is given. (c) Map of the measured out-of-plane mistilt. (d) Map of estimated error of the tilt measurement. Blue regions F and G in (a) are compared in Fig. 7 and discussed in the text to explain local failure of Kikuchi band detection.

4.2. Bending of specimens at large fields of view

Fig. 6(a) shows the ADF signal obtained from 4D-STEM data at a scan raster of 400×3500, which corresponds to a field of view of 17 nm $\times$ 146 nm. The left-hand side contains an epitaxial $La_{0.7}Sr_{0.3}MnO_3$ layer (bright), grown on an $SrTiO_3$ substrate on the right hand side [52]. Subsets of the data are shown in Fig. 6(b) for five substrate regions A-E labeled in (a), being approximately 30 nm apart from each other.

Although atomic resolution is present in all ADF images, their contrast varies significantly and is maximum in regions C and D, which correspond to an approximate zone axis condition. A selection of PACBED patterns from different regions of the scan is displayed in Fig. 6(b). In particular, a variation of crystal tilt is identified therein by the apparent vertical shift of the crossing of the Kikuchi bands when comparing the patterns in sequence from region A to region E. In the example patterns shown, green dots mark the Kikuchi bands detected by the automated mistilt measurement. The measurement routine provides an internal error estimate σ which corresponds to the root-mean-squared (r.m.s.) deviation of line crossings found in the analysis, e.g., as shown in Fig. 3. Error estimates in this experimental study are well below one milliradian, whereas the mistilt magnitude from [100] zone axis reaches up to 9 mrad in some regions.

From the scan a set of 40 × 350 PACBED patterns was generated, where each PACBED is calculated from an area corresponding to one projected pseudo-cubic unit of the perovskite. The application of the iterative evaluation procedure took 20 min in total on a consumer-grade computer. The result of the systematic mistilt analysis for the whole region of Fig. 6(a) is shown in Fig. 6(c). A color scale is used to display the modulus and direction of mistilt in terms of brightness and hue, respectively. The change from blue to green along the vertical scanning direction corresponds to a change of the vertical tilt component. This dominant variation of tilt is approximately a linear function of the scan position and corresponds to a bending of the specimen around a horizontal axis by approximately ±9 mrad, as plotted in Fig. 7.

Although the global trend of the tilt variation is linear, significant local deviations from this trend are observed in the epitaxial layer. These areas also appear with higher brightness in the ADF image of Fig. 6(a). A map of the measurement error estimated by the automated procedure is plotted in Fig. 6(d). A good precision of 0.3 to 0.6 mrad is obtained in the substrate while the majority of measurements in the epitaxial layer has an error below 2 mrad. Significantly larger errors are found in some areas of the epitaxial layer, especially at the bottom of the map, where also the measured tilts scatter strongly. This indicates that the algorithm could not converge in these cases within a predefined limit of 30 iterations, most likely due to a low contrast of the Kikuchi-band pattern.

To shed light on the origin of the failure of Kikuchi band detection in such regions, as seen predominantly in Fig. 6(c) bottom left, average diffraction patterns have been calculated in the blue regions F and G in Fig. 6(a) and added as insets to Fig. 7. Obviously, region F causes stronger diffuse scattering within the recorded dark field region than region G, and lacks Kikuchi bands nearly completely. This could be indicative for preparation-induced redeposition of amorphous specimen material on the surface, whereas this would then also be expected more prominently in substrate regions. Another explanation could be additional diffuse intensity due to Huang scattering [53] associated with disorder in the bulk, which also hampers Kikuchi band detection by lowering their contrast. Note that the first Laue zone lies beyond the recorded solid angle range and should thus have no significant impact on the evaluation.

It is instructive to interpret the obtained tilt map in terms of strain-induced tilt variations caused by the epitaxial layer grown with a lattice mismatch of 0.8%. For this purpose, we calculated a line profile of the mistilt along the direction indicated by the green arrow in Fig. 6(a) separately for the substrate and epitaxial layer. These line profiles are plotted in Fig. 7 for (a) the component of tilt perpendicular to the interface and (b) the component of tilt parallel to the interface. The blue profile was measured from substrate areas and shows a constant bending of the lamella along the interface with a tilt gradient of 143 μrad/nm and a standard deviation of 1 mrad, as indicated by error bars. In contrast to that, the red curves measured on the layer material show a wave-like deviation from the linear trend of up to 7 mrad, which are likely caused by thin foil relaxation and defects. Larger error bars of the layer measurement reflect both, the slightly worse precision of tilt detection and an increased tilt variation in the layer material also along the direction perpendicular to the interface.
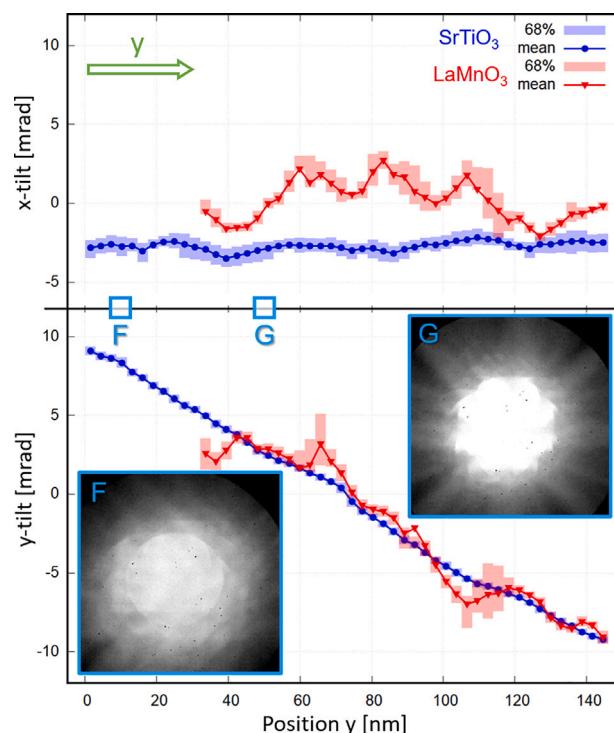

Fig. 7. Line profiles of sample mistilt along the arrow in Fig. 6 in the epitaxial layer (red) and the substrate (blue). (a) Mistilt x-component, perpendicular to the interface, and (b) y-component, parallel to the interface, show a different variation with sample position. Whereas there is almost no change of the x-component, the y component exhibits a linear trend, indicating sample bending of 20 mrad over 140 nm. Oscillations of the sample mistilt around the linear trend are observed in the epitaxial layer for both components. The first 30 nm in the epitaxial layer could not be evaluated as seen in Fig. 6c (bottom left). The reason is seen directly in the average diffraction patterns F and G corresponding to the blue regions in Fig. 6a, revealing a lack of Kikuchi bands in region F as discussed in the text.

4.3. Tilt measurement in high-Mn steel

The second case study is a tilt mapping across a twin boundary in austenitic steel. The results in Fig. 8 show the mapping of a perfect $\Sigma 3$ twin boundary viewed along the common [110] direction of the two grains with the twin boundary in a {111} plane and oriented horizontally in Fig. 8(a). From the methodological point of view, this structure is interesting since it provides an interface of a perfect twin which is well understood, however, without adding complexity due to compositional gradients or strain. Besides mapping the tilt induced by bending of the thinned TEM sample, as in the previous case, this second case provides additional insight regarding the attainable spatial resolution of the tilt measurement, because the crystallographic orientation changes abruptly at the twin boundary. The change of orientation is apparent in the PACBED patterns as an in-plane mirror with respect to the [111] interface plane, which is marked by the dashed line in Fig. 8(b).

Fig. 8(c) shows the orientation map in a scan of 14 nm × 14 nm. The sample appears mostly flat with tilt variations of 1 to 2 mrad. Although these orientation changes are small, they are smooth across the twin boundary and measured with very good precision of $\sigma < 0.1$ mrad. Above this level of uncertainty, no abrupt change of the out-of-plane crystallographic orientation was found at the grain boundary. This indicates that the two grains are indeed perfect crystallization twins.

Pattern B displays an obvious problem for the procedure of tilt measurement at grain boundaries with significant orientation changes. There are partial bands on either side of the {111} plane, i.e. no counterpart is found on the opposite side to support a pair-wise relation

(a)

A

B

2 nm

C

(b) A   B   C

(c) Tilt [mrad]

-2

0

2

-2 0 2
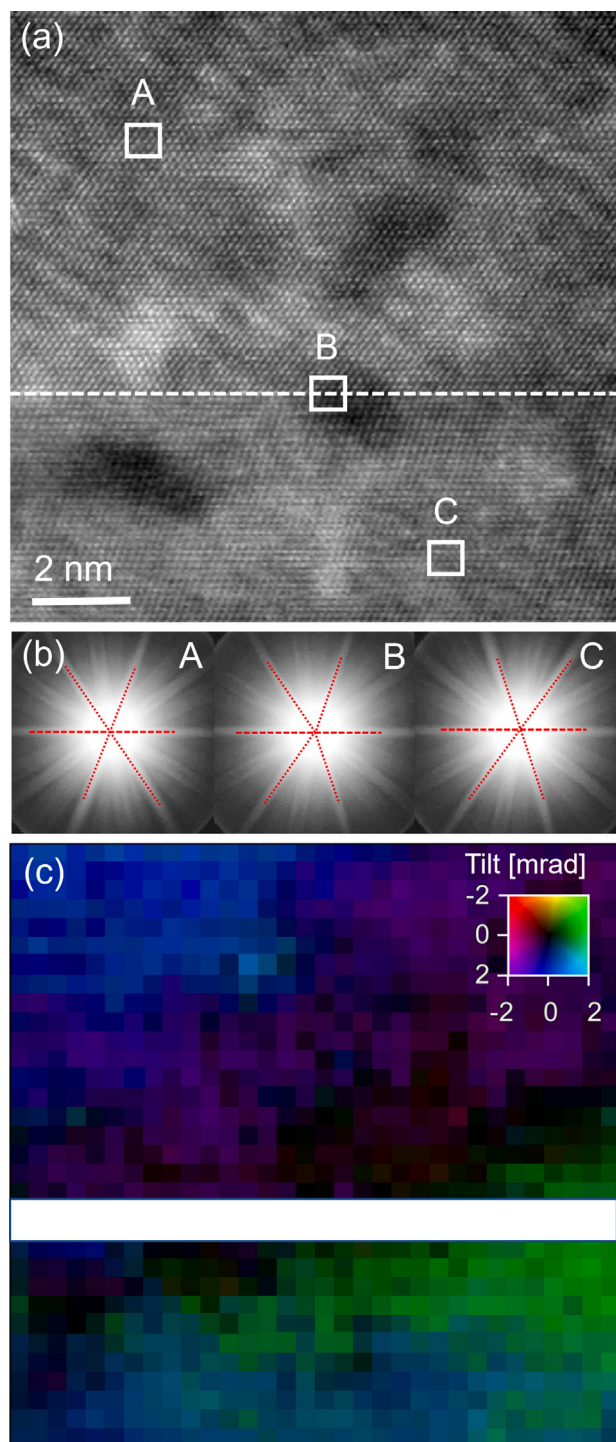
Fig. 8. Mistilt mapping across a perfect twin boundary in high-Mg steel. (a) Virtual ADF image calculated from the 4D-STEM data set. Two grains with different in-plane orientation are separated by a horizontal grain boundary. (b) Example PACBED patterns of three selected areas from (a) with positions A and C taken on either side of the boundary and B taken from an area that includes the boundary. (c) Out-of-plane orientation map showing a small sample bending of approximately 2 mrad over the entire field of view.

with good accuracy and precision, i.e. the mistilt at these positions does not deviate much from the results obtained deeper in the grains, and the error estimates are likewise small. Accordingly, we deduce that the result in one grain is not influenced by the difference in orientation of the other grain at a distance of two unit cells, which could be interpreted as a spatial resolution of better than 0.8 nm in this case.
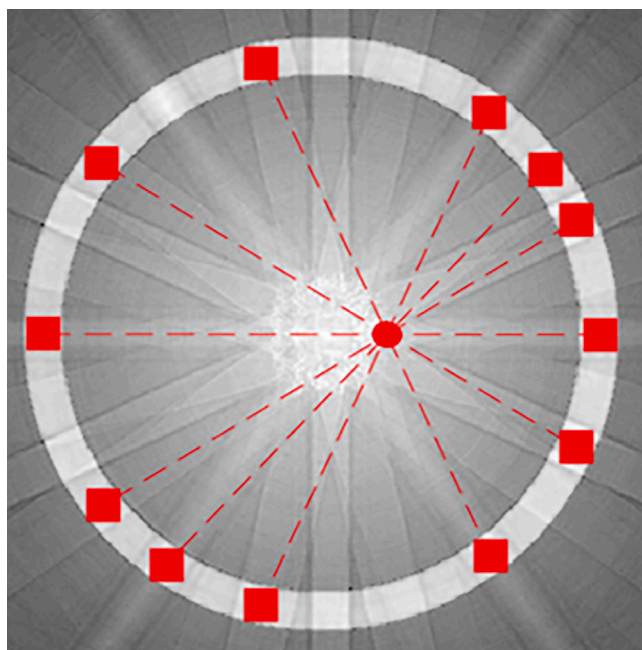
5. Discussion

A geometric approach to measure crystal orientation from diffraction patterns has been presented. By choosing Kikuchi bands as the source of the signal for orientation mistilt measurement, the evaluation procedure requires that Kikuchi bands are separated from other much stronger features in electron diffraction patterns, such as the bright field and Bragg reflections. A sufficiently large sample thickness is required, in most cases more than 10 nm, to generate significant Kikuchi bands at room temperature. The purpose of the method is to measure mistilt in orientations close to a high symmetry zone axis as frequently used in high-resolution STEM. In principle it is beneficial for the geometric analysis that the diffraction pattern covers a large angular range which can be achieved by choosing a short camera length. In our experiments the method produced reliable results in cases where the bright-field diameter is smaller than half the edge length of the detector. In addition, shorter camera lengths allow for larger mistilts to be analyzed and better precision. A compromise should be found when extending the angular range of detection because the signal drops towards larger angles (decay of scattering factors) and non-linear projection distortions can complicate angular calibration. Even on simulated patterns, as well as under optimized experimental conditions we found a limitation of precision of about 0.1 mrad root-mean-square for the mistilt which is mainly due to the finite width of the Kikuchi bands.

It is instructive to study whether Kikuchi band detection is facilitated by heating specimens. Simulations show the disappearance of higher-order Laue-zone (HOLZ) rings with increasing temperature, which may otherwise lead to systematic errors or failures of the procedure. In particular, this would be the case when at least one HOLZ ring is partially but not completely included in the azimuthal scan. The diffuse scattering signal increases with increasing sample temperature on the one hand. However, the simulations do not show a likewise increased contrast of Kikuchi bands on the other hand. Apart from the disappearance of the HOLZ signal, heating the sample does not seem to offer significant advantages.

At lower beam energies and large mistilt Kikuchi bands can appear curved in the diffraction pattern, since their edges follow conic sections in the strict sense. As a consequence, the prediction of the crossing point of the bands with the present method could become slightly inaccurate. In this case, a final step evaluating the full two-dimensional course of the Kikuchi bands could be necessary, e.g., assuming hyperbolic shapes. However, in the cases presented here, sufficiently high beam energies have been used such that this error is negligible.

A significant step in the pattern analysis is reducing a two-dimensional problem, the intersection of bands, to a one-dimensional problem, measuring peak positions in an azimuthal intensity profile. This is beneficial for the speed and complexity of the numerical evaluation. However, a problem may arise when associating pairs of peaks to bands. The smallest root-mean-square distance of band intersections is used as the main criterion for finding the correct association. There are rare cases, even under good experimental conditions, where this criterion yields a deceptively good but actually wrong result. An example is depicted in Fig. 9. Note that the computer only operates based on the 1D scan and does not perceive the 2D pattern like a human observer. These initially wrong results are, however, healed by the refinement step using another azimuthal scan extracted from a different area of the 2D pattern. In all cases observed so far, this procedure converged to the correct result. It follows from the purely geometrical evaluation and

of peaks in the azimuthal scan to a Kikuchi band. This causes the measurement routine to fail, which is reflected by the white area at the twin boundary in Fig. 8(c). The width of the white area corresponds to that of one unit cell on either side of the twin boundary. Already at a distance of two unit cells from the boundary, the routine works well

Fig. 9. Simulated PACBED pattern of Fe [110] fcc steel and example of a false detection of the Kikuchi band intersection with a very small root-mean-square deviation. This is a rare case, where by chance, the depicted wrong association of pairs of peaks to bands leads to the smallest deviation of common intersections. Given the underlying 2-dimensional pattern, the error is obvious, but not detectable in the evaluation of a single azimuthal scan. Using the iterative scheme, this false detection is nevertheless eliminated.

the reduction to a one-dimensional problem, that the method can in fact detect the rotation and position of a cross generically, however, it does not exploit physical constraints that could, e.g., identify the indices of a zone axis or false mirror planes.

Applying the method to 4D-STEM data allows for mapping local mistilt. The two experimental case studies presented in the results section both show systematic variations in local orientation. Each pixel in the maps corresponds to a scanned area from which diffraction patterns have been averaged and then analyzed independently. The locality of tilt information, however, needs to be interpreted with care due to the significant thickness- and orientation-dependent broadening of the electron probe in the specimen. An empirical assessment of the spatial resolution for mistilt variation is found in the mapping of Fig. 8 for a perfect twin-boundary in steel. Already at a distance of one unit cell from the twin boundary to either side, the measured tilts are consistent with the rest of the grain, which suggests that the mistilt information is generated from a projected area with a radius of approximately one unit cell in the present case. For patterns generated from areas closer to the grain boundary, e.g. pattern B in Fig. 8(b), the method fails for obvious reasons. In this case all Kikuchi bands except one terminate at the pole and do not generate the expected signal on the opposite side of the azimuthal scan. In the case of high-resolution STEM of steel, a continuous Kikuchi band along a direction is therefore generated as soon as there is at least one atomic column from the scan position in both directions to form a crystal plane. For the most intense Kikuchi bands, the neighboring columns have distances of one or two unit cells. The spatial resolution for local tilt mapping is therefore determined by the spacing of atomic columns in the crystallographic planes corresponding to the Kikuchi bands used in the analysis. Since all orientation mappings presented in this study were generated from PACBED patterns of at least unit cell areas, tilt information in one data point can be seen as independent from its neighbors.

6. Summary and conclusion

To measure small tilts from the zone axis geometry, an approach based on the signal from Kikuchi bands in diffraction patterns was chosen. This approach requires a minimum of a-priori information and can thus be used with little preliminary work. The need to record Kikuchi bands does not preclude simultaneous evaluation of bright field or elastic diffraction signal as long as both are recorded with sufficient area on the detector. This means that, for example, with a momentum-resolved STEM measurement (4D-STEM), data relevant to material science as well as supporting data important for later modeling, such as tilt, can be recorded simultaneously.

The evaluation procedure has been implemented numerically and provides fast and reliable results with accuracy on the order of 0.1 mrad mistilt. However, the application of the method to typical (S)TEM diffraction patterns is limited to small mistilts of less than 5° and requires a crystal thickness sufficient to form Kikuchi bands. As a further development it could be investigated whether the need for minimal inputs can be completely avoided, e.g. by training a neural network with multiple patterns, to obtain a fully automatic method.

Two examples have demonstrated that the method can be used to map sample mistilts over large areas and interfaces. The resulting information allows for the measurement of orientation changes across interfaces and to determine grain boundary parameters. This is important in modeling, e.g., when diffraction effects need to be separated from that of chemical gradients. The high speed of the evaluation allows fast feedback for an online sample-tilt optimization. This would be a step towards automating high resolution transmission electron microscopy in finding zone-axis orientation or applying deliberate mistilts for, e.g., quantitative EDX.

CRediT authorship contribution statement

Mauricio Cattaneo: Writing – original draft, Visualization, Software, Investigation, Data curation. **Knut Müller-Caspary:** Writing – review & editing, Writing – original draft, Validation, Supervision, Software, Project administration, Methodology, Investigation, Funding acquisition, Formal analysis, Data curation, Conceptualization. **Juri Barthel:** Writing – review & editing, Writing – original draft, Supervision, Software, Methodology, Investigation, Funding acquisition, Formal analysis, Data curation, Conceptualization. **Katherine E. MacArthur:** Supervision, Investigation. **Nicolas Gauquelin:** Investigation, Data curation. **Marta Lipinska-Chwalek:** Investigation, Formal analysis, Data curation, Conceptualization. **Johan Verbeeck:** Writing – review & editing, Resources, Project administration, Funding acquisition, Formal analysis, Conceptualization. **Leslie J. Allen:** Writing – review & editing, Supervision, Funding acquisition. **Rafal E. Dunin-Borkowski:** Writing – review & editing, Supervision, Resources, Project administration, Funding acquisition, Conceptualization.

Declaration of competing interest

The authors declare that they have no known competing financial interests or personal relationships that could have appeared to influence the work reported in this paper.

Data availability

Data will be made available on request.

Acknowledgments

Appendix. Calculation of line crossings from positions in an azimuthal scan

Given is a list of $2n$ unequal azimuthal angles φ_i corresponding to positions

$$\mathbf{X}_i = \mathbf{Q} + r \begin{pmatrix} \cos\varphi_i \\ \sin\varphi_i \end{pmatrix} \tag{A.1}$$

on a circle of radius r with center $\mathbf{Q}$ in a two-dimensional plane. The list is sorted, such that $\varphi_i < \varphi_{i+1}$ for all $i \geq 1$ and $i < 2n$. n lines are constructed by connecting pairs of positions $\mathbf{X}_i$ and $\mathbf{X}_{i+n}$ for $i \leq n$. A line that contains two points $\mathbf{X}_i$ and $\mathbf{X}_j$ is given by the formula

$$\mathbf{L}_{ij}(t) = \mathbf{X}_i + t(\mathbf{X}_j - \mathbf{X}_i), t \in \mathbb{R}. \tag{A.2}$$

The crossing point of two different lines $\mathbf{L}_{ij}(t_1)$ and $\mathbf{L}_{kl}(t_2)$ with $k \neq i$, $j = i + n$, and $l = k + n$ is found by solving the system of two equations given by

$$0 = \mathbf{L}_{ij}(t_1) - \mathbf{L}_{kl}(t_2) \tag{A.3}$$

for the parameters t_1 and t_2 and calculating the respective position via Eq. (A.2). The solution is found as

$$\begin{pmatrix} t_1 \\ t_2 \end{pmatrix} = A^{-1}\mathbf{B}, \tag{A.4}$$

with the 2×2 matrix A given by

$$A = \begin{pmatrix} \mathbf{X}_j - \mathbf{X}_i & \mathbf{X}_k - \mathbf{X}_l \end{pmatrix} \tag{A.5}$$

and the right side vector

$$\mathbf{B} = \mathbf{X}_k - \mathbf{X}_i. \tag{A.6}$$

References

[1] S.J. Pennycook, L.A. Boatner, Chemically sensitive structure-imaging with a scanning transmission electron microscope, Nature 336 (1988) 565–567, http://dx.doi.org/10.1038/336565a0.

[2] S.D. Findlay, N. Shibata, H. Sawada, E. Okunishi, Y. Kondo, Y. Ikuhara, Dynamics of annular bright field imaging in scanning transmission electron microscopy, Ultramicroscopy 110 (2010) 903–923, http://dx.doi.org/10.1016/j.ultramic.2010.04.004.

[3] M. Bosman, V.J. Keast, J.L. Garcia-Munoz, A.J. D'Alfonso, S.D. Findlay, L.J. Allen, Two-dimensional mapping of chemical information at atomic resolution, Phys. Rev. Lett. 99 (8) (2007) 086102, http://dx.doi.org/10.1103/PhysRevLett.99.086102.

[4] A.J. D'Alfonso, B. Freitag, D. Klenov, L.J. Allen, Atomic-resolution chemical mapping using energy-dispersive X-ray spectroscopy, Phys. Rev. B 81 (10) (2010) 100101, http://dx.doi.org/10.1103/PhysRevB.81.100101.

[5] S.E. Maccagnano-Zacher, K.A. Mkhoyan, E.J. Kirkland, J. Silcox, Effects of tilt on high-resolution ADF-STEM imaging, Ultramicroscopy 108 (8) (2008) 718–726, http://dx.doi.org/10.1016/j.ultramic.2007.11.003.

[6] D. Zhou, K. Müller-Caspary, W. Sigle, F.F. Krause, A. Rosenauer, P.A. van Aken, Sample tilt effects on atom column position determination in ABF–STEM imaging, Ultramicroscopy 160 (2016) 110–117, http://dx.doi.org/10.1016/j.ultramic.2015.10.008.

[7] K.E. MacArthur, A.B. Yankovich, A. Béché, M. Luysberg, H.G. Brown, S.D. Findlay, M. Heggen, L.J. Allen, Optimizing experimental conditions for accurate quantitative energy-dispersive X-ray analysis of interfaces at the atomic scale, Microsc. Microanal. 27 (2021) 528–542, http://dx.doi.org/10.1017/S1431927621000246.

[8] K.E. MacArthur, H.G. Brown, S.D. Findlay, L.J. Allen, Probing the effect of electron channelling on atomic resolution energy dispersive X-ray quantification, Ultramicroscopy 182 (2017) 264–275, http://dx.doi.org/10.1016/j.ultramic.2017.07.020.

[9] N.R. Lugg, G. Kothleitner, N. Shibata, Y. Ikuhara, On the quantitativeness of EDS STEM, Ultramicroscopy 151 (2015) 150–159, http://dx.doi.org/10.1016/j.ultramic.2014.11.029.

[10] Z. Chen, Y. Jiang, Y.-T. Shao, M.E. Holtz, M. Odstrčil, M. Guizar-Sicairos, I. Hanke, S. Ganschow, D.G. Schlom, D.A. Muller, Electron ptychography achieves atomic-resolution limits set by lattice vibrations, Science 372 (6544) (2021) 826–831, http://dx.doi.org/10.1126/science.abg2533, arXiv:https://science.sciencemag.org/content/372/6544/826.full.pdf, URL https://science.sciencemag.org/content/372/6544/826.

[11] H. Sha, Y. Ma, G. Cao, J. Cui, W. Yang, Q. Li, R. Yu, Sub-nanometer-scale mapping of crystal orientation and depth-dependent structure of dislocation cores in SrTiO$_3$, Nature Commun. 14 (1) (2023) 162, http://dx.doi.org/10.1038/s41467-023-35877-7.

[12] B. Diederichs, Z. Herdegen, A. Strauch, F. Filbir, K. Müller-Caspary, Exact inversion of partially coherent dynamical electron scattering for picometric structure retrieval, Nature Commun. 15 (1) (2024) 101, http://dx.doi.org/10.1038/s41467-023-44268-x.

[13] W. Van den Broek, C.T. Koch, Method for retrieval of the three-dimensional object potential by inversion of dynamical electron scattering, Phys. Rev. Lett. 109 (2012) 245502, http://dx.doi.org/10.1103/PhysRevLett.109.245502, URL https://link.aps.org/doi/10.1103/PhysRevLett.109.245502.

[14] Z. Liao, N. Gauquelin, R.J. Green, K. Müller-Caspary, I. Lobato, L. Li, S.V. Aert, J. Verbeeck, M. Huijben, M.N. Grisolia, V. Rouco, R. El Hage, J.E. Villegas, A. Mercy, M. Bibes, P. Ghosez, G.A. Sawatzky, G. Rijnders, G. Koster, Metal–insulator-transition engineering by modulation tilt-control in perovskite nickelates for room temperature optical switching, Proc. Natl. Acad. Sci. 115 (38) (2018) 9515–9520, http://dx.doi.org/10.1073/pnas.1807457115.

[15] M. Calcagnotto, D. Ponge, E. Demir, D. Raabe, Orientation gradients and geometrically necessary dislocations in ultrafine grained dual-phase steels studied by 2d and 3d EBSD, Mater. Sci. Eng. A 527 (10) (2010) 2738–2746, http://dx.doi.org/10.1016/j.msea.2010.01.004.

[16] A. Strauch, B. März, T. Denneulin, M. Cattaneo, A. Rosenauer, K. Müller-Caspary, Systematic errors of electric field measurements in ferroelectrics by unit cell averaged momentum transfers in STEM, Microsc. Microanal. 29 (2023) 499–511, http://dx.doi.org/10.1093/micmic/ozad016.

[17] K. Müller, H. Ryll, I. Ordavo, S. Ihle, L. Strüder, K. Volz, J. Zweck, H. Soltau, A. Rosenauer, Scanning transmission electron microscopy strain measurement from millisecond frames of a direct electron charge coupled device, Appl. Phys. Lett. 101 (2012) 212110, http://dx.doi.org/10.1063/1.4767655.

[18] R. Plackett, I. Horswell, E.N. Gimenez, J. Marchal, D. Omar, N. Tartoni, Merlin: a fast versatile readout system for Medipix3, J. Instrum. 8 (2013) C01038, http://dx.doi.org/10.1088/1748-0221/8/01/C01038.

[19] K. Müller-Caspary, A. Oelsner, P. Potapov, Two-dimensional strain mapping in semiconductors by nano-beam electron diffraction employing a delay-line detector, Appl. Phys. Lett. 107 (2015) 072110, http://dx.doi.org/10.1063/1.4927837.

[20] H. Ryll, M. Simson, R. Hartmann, P. Holl, M. Huth, S. Ihle, Y. Kondo, P. Kotula, A. Liebel, K. Müller-Caspary, A. Rosenauer, R. Sagawa, J. Schmidt, H. Soltau, L. Strüder, A pnCCD-based, fast direct single electron imaging camera for TEM and STEM, J. Instrum. 11 (2016) P04006, http://dx.doi.org/10.1088/1748-0221/11/04/P04006.

[21] M.W. Tate, P. Purohit, D. Chamberlain, K.X. Nguyen, R. Hovden, C.S. Chang, P. Deb, E. Turgut, J.T. Heron, D.G. Schlom, D.C. Ralph, G.D. Fuchs, K.S. Shanks, H.T. Philipp, D.A. Muller, S.M. Gruner, High dynamic range pixel array detector for scanning transmission electron microscopy, Microsc. Microanal. 22 (2016) 237–249, http://dx.doi.org/10.1017/S1431927615015664.

[22] D. Jannis, C. Hofer, C. Gao, X. Xie, A. Béché, T.J. Pennycook, J. Verbeeck, Event driven 4D STEM acquisition with a Timepix3 detector: Microsecond dwell time and faster scans for high precision and low dose applications, Ultramicroscopy 233 (2022) 113423, http://dx.doi.org/10.1016/j.ultramic.2021.113423.

[23] W. Xu, J.M. LeBeau, A deep convolutional neural network to analyze position averaged convergent beam electron diffraction patterns, Ultramicroscopy 188 (2018) 59–69, http://dx.doi.org/10.1016/j.ultramic.2018.03.004.

[24] J.M. LeBeau, S.D. Findlay, L.J. Allen, S. Stemmer, Position averaged convergent beam electron diffraction: Theory and applications, Ultramicroscopy 110 (2010) 118–125, http://dx.doi.org/10.1016/j.ultramic.2009.10.001.

[25] S. Nishikawa, S. Kikuchi, Diffraction of cathode rays by mica, Nature 121 (3061) (1928) 1019–1020, http://dx.doi.org/10.1038/1211019a0.

[26] B.L. Adams, S.I. Wright, K. Kunze, Orientation imaging: The emergence of a new microscopy, Metall. Trans. A 24 (4) (1993) 819–831, http://dx.doi.org/10.1007/BF02656503.

[27] S.I. Wright, B.L. Adams, Automatic analysis of electron backscatter diffraction patterns, Metall. Trans. A 23 (3) (1992) 759–767, http://dx.doi.org/10.1007/BF02675553.

[28] S. Däbritz, E. Langer, W. Hauffe, Kossel and pseudo Kossel CCD pattern in comparison with electron backscattering diffraction diagrams, Appl. Surf. Sci. 179 (1) (2001) 38–44, http://dx.doi.org/10.1016/S0169-4332(01)00260-4, 11th Conference on Applied Surface Science. URL https://www.sciencedirect.com/science/article/pii/S0169433201002604.

[29] J.A. Venables, C.J. Harland, Electron back-scattering patterns — A new technique for obtaining crystallographic information in the scanning electron microscope, Phil. Mag.: J. Theor. Exp. Appl. Phys. 27 (5) (1973) 1193–1200, http://dx.doi.org/10.1080/14786437308225827.

[30] P.W. Trimby, Orientation mapping of nanostructured materials using transmission Kikuchi diffraction in the scanning electron microscope, Ultramicroscopy 120 (2012) 16–24, http://dx.doi.org/10.1016/j.ultramic.2012.06.004.

[31] G.L. Burton, S. Wright, A. Stokes, D.R. Diercks, A. Clarke, B.P. Gorman, Orientation mapping with kikuchi patterns generated from a focused stem probe and indexing with commercially available EDAX software, Ultramicroscopy 209 (2020) 112882, http://dx.doi.org/10.1016/j.ultramic.2019.112882.

[32] S.I. Wright, D.J. Dingley, Orientation imaging in the transmission electron microscope, in: Texture and Anisotropy of Polycrystals, in: Materials Science Forum, vol. 273, Trans Tech Publications Ltd, 1998, pp. 209–214, http://dx.doi.org/10.4028/www.scientific.net/MSF.273-275.209.

[33] D.J. Dingley, Extension of orientation mapping to the transmission electron microscope, in: Textures of Materials - ICOTOM 14, in: Materials Science Forum, vol. 495, Trans Tech Publications Ltd, 2005, pp. 225–230, http://dx.doi.org/10.4028/www.scientific.net/MSF.495-497.225.

[34] S. Zaefferer, New developments of computer-aided crystallographic analysis in transmission electron microscopy, J. Appl. Crystallogr. 33 (1) (2000) 10–25, http://dx.doi.org/10.1107/S0021889899010894.

[35] S. Zaefferer, High resolution crystal orientation measurement techniques for the study of nucleation processes during recrystallization in heavily deformed metals, Rev. Mét. 100 (9) (2003) 891–901, http://dx.doi.org/10.1051/metal:2003213.

[36] D.J. Dingley, Orientation imaging microscopy for the transmission electron microscope, Microchim. Acta 155 (1) (2006) 19–29, http://dx.doi.org/10.1007/s00604-006-0502-4.

[37] J. Fundenberger, E. Bouzy, D. Goran, J. Guyon, H. Yuan, A. Morawiec, Orientation mapping by transmission-sem with an on-axis detector, Ultramicroscopy 161 (2016) 17–22, http://dx.doi.org/10.1016/j.ultramic.2015.11.002, URL https://www.sciencedirect.com/science/article/pii/S0304399115300656.

[38] M.U. Farooq, R. Villaurrutia, I. MacLaren, H. Kungl, M.J. Hoffmann, J.-J. Fundenberger, E. Bouzy, Using EBSD and TEM-Kikuchi patterns to study local crystallography at the domain boundaries of lead zirconate titanate, J. Microsc. 230 (3) (2008) 445–454, http://dx.doi.org/10.1111/j.1365-2818.2008.02004.x, arXiv:https://onlinelibrary.wiley.com/doi/pdf/10.1111/j.1365-2818.2008.02004.x, URL https://onlinelibrary.wiley.com/doi/abs/10.1111/j.1365-2818.2008.02004.x.

[39] C. Maurice, R. Fortunier, A 3d hough transform for indexing ebsd and kossel patterns, J. Microsc. 230 (3) (2008) 520–529, http://dx.doi.org/10.1111/j.1365-2818.2008.02045.x, arXiv:https://onlinelibrary.wiley.com/doi/pdf/10.1111/j.1365-2818.2008.02045.x, URL https://onlinelibrary.wiley.com/doi/abs/10.1111/j.1365-2818.2008.02045.x.

[40] N. Krieger Lassen, D. Juul Jensen, K. Conradsen, Image processing procedures for analysis of electron back scattering patterns, Scanning Microsc. 6 (1) (1992) 115–121.

[41] A. Silinga, C.S. Allen, J. Barthel, C. Ophus, I. MacLaren, Measurement of atomic modulation direction using the azimuthal variation of first-order laue zone electron diffraction, Microsc. Microanal. 29 (5) (2023) 1682–1687, http://dx.doi.org/10.1093/micmic/ozad089, arXiv:https://academic.oup.com/mam/article-pdf/29/5/1682/51889153/ozad089.pdf.

[42] L. Reimer, H. Kohl, Transmission Electron Microscopy, Springer, New York, NY, 2008, http://dx.doi.org/10.1007/978-0-387-40093-8.

[43] J.M. Cowley, A.F. Moodie, The scattering of electrons by atoms and crystals. I. A new theoretical approach, Acta Crystallogr. 10 (10) (1957) 609–619, http://dx.doi.org/10.1107/S0365110X57002194.

[44] J. Barthel, Dr. Probe: A software for high-resolution STEM image simulation, Ultramicroscopy 193 (2018) 1–11, http://dx.doi.org/10.1016/j.ultramic.2018.06.003.

[45] B.D. Forbes, A.V. Martin, S.D. Findlay, A.J. D'Alfonso, L.J. Allen, Quantum mechanical model for phonon excitation in electron diffraction and imaging using a Born-Oppenheimer approximation, Phys. Rev. B 82 (2010) 104103, http://dx.doi.org/10.1103/PhysRevB.82.104103.

[46] M.E. Straumanis, D.C. Kim, Lattice constants, thermal expansion coefficients, densities and perfection of structure of pure iron and of iron loaded with hydrogen, Int. J. Mater. Res. 60 (4) (1969) 272–277, http://dx.doi.org/10.1515/ijmr-1969-600404.

[47] L.-M. Peng, G. Ren, S.L. Dudarev, M.J. Whelan, Debye–Waller factors and absorptive scattering factors of elemental crystals, Acta Crystallogr. Sect. A 52 (3) (1996) 456–470, http://dx.doi.org/10.1107/S010876739600089X.

[48] Ernst Ruska-centre for microscopy and spectroscopy with electrons (ER-C), Fei titan 80-300 stem, J. Large-Scale Res. Facil. 2 (2016) A42, http://dx.doi.org/10.17815/jlsrf-2-67.

[49] Ernst Ruska-centre for microscopy and spectroscopy with electrons (ER-C), Fei titan g2 80-200 crewley, J. Large-Scale Res. Facil. 2 (2016) A43, http://dx.doi.org/10.17815/jlsrf-2-68.

[50] G.W. Paterson, R.J. Lamb, R. Ballabriga, D. Maneuski, V. O'Shea, D. McGrouther, Sub-100 nanosecond temporally resolved imaging with the Medipix3 direct electron detector, Ultramicroscopy 210 (2020) 112917, http://dx.doi.org/10.1016/j.ultramic.2019.112917.

[51] M. Kruth, D. Meertens, K. Tillmann, FEI helios nanolab 460f1 fib-sem, J. Large-Scale Res. Facil. JLSRF 2 (2016) http://dx.doi.org/10.17815/jlsrf-2-105.

[52] M. Keunecke, F. Lyzwa, D. Schwarzbach, V. Roddatis, N. Gauquelin, K. Müller-Caspary, J. Verbeeck, S.J. Callori, F. Klose, M. Jungbauer, V. Moshnyaga, High-t_C interfacial ferromagnetism in $srmno_3/lamno_3$ superlattices, Adv. Funct. Mater. 30 (18) (2020) 1808270, http://dx.doi.org/10.1002/adfm.201808270.

[53] K. Huang, X-ray reflexions from dilute solid solutions, Proc. R. Soc. Lond. Ser. A 190 (1020) (1947) 102–117, http://dx.doi.org/10.1098/rspa.1947.0064.